A Constrained Solver for Optical Absorption Tomography

NICK POLYDORIDES[1*], ALEX TSEKENIS[1], EDWARD FISHER[1], ANDREA CHIGHINE[1], HUGH MCCANN[1], LUCA DIMICCOLI[2], PAUL WRIGHT[3], MICHAEL LENGDEN[4], THOMAS BENOY[4], DAVID WILSON[4], GORDON HUMPHRIES[4], AND WALTER JOHNSTONE[4]

[1] School of Engineering, Institute for Digital Communications, University of Edinburgh, Edinburgh, UK.
[2] Department of Electronics and Informatics, Vrije University Brussels, Brussels, Belgium.
[3] School of Electrical & Electronic Engineering, University of Manchester, Manchester, UK.
[4] Department of Engineering, Photonics, Strathclyde University, Glasgow, UK.
[*] Corresponding author: n.polydorides@ed.ac.uk

Compiled September 25, 2017

We consider the inverse problem of concentration imaging in optical absorption tomography with limited data sets. The measurement setup involves simultaneous acquisition of near infrared wavelength-modulated spectroscopic measurements from a small number of pencil beams equally distributed among six projection angles surrounding the plume. We develop an approach for image reconstruction that involves constraining the value of the image to the conventional concentration bounds and a projection into low-dimensional subspaces to reduce the degrees of freedom in the inverse problem. Effectively, by re-parameterising the forward model we impose simultaneously spatial smoothness and a choice between three types of inequality constraints, namely positivity, boundedness and logarithmic boundedness in a simple way that yields an unconstrained optimisation problem in a new set of surrogate parameters. Testing this numerical scheme with simulated and experimental phantom data indicates that the combination of affine inequality constraints and subspace projection leads to images that are qualitatively and quantitatively superior to unconstrained regularised reconstructions. This improvement is more profound in targeting concentration profiles of small spatial variation. We present images and convergence graphs from solving these inverse problems using Gauss-Newton's algorithm to demonstrate the performance and convergence of our method.

OCIS codes: *(110.1758) Computational imaging; (110.6960) Tomography; (120.1740) Combustion diagnostics*

http://dx.doi.org/10.1364/ao.XX.XXXXXX

1. INTRODUCTION

Chemical Species Tomography (CST) aims to image the concentration of chemical species present in gas mixtures [1]. Its application to carbon dioxide (CO_2) in gas turbine aero-engine exhausts is motivated by the aviation industry's need to reduce CO_2 emissions and to enable the analysis of emissions data in order to diagnose engine condition [2], [3]. As CO_2 is a major product of the combustion process, it provides a good proxy to understand the complex phenomena that govern the performance of advanced gas turbines and predict irregularities and faults. Moreover, imaging the concentration of carbon dioxide in a jet's exhaust plume enables the assessment of the performance of novel aviation fuels at full-scale operating conditions. CST was initially inspired by the success of X-ray computed tomography, and has since been developed into an optical imaging modality for gas tomography suitable to the cases where photon transmission and absorption phenomena dominate those of scattering and diffusion. Over the recent years, collimated pencil, fan or ad hoc beam arrangements have been proposed [4], and rapid developments have seen CST evolve from the monochromatic to the hyperspectral setting exploiting advances in calibration-free 2f/1f wavelength modulation spectroscopy technique (TDLS-WMS), see for example [5], [6], [7] and [8]. While measurement models involve invariably computation of line integrals under some assumptions based on the experimental conditions, the acquisition of spectral measurements has paved the way for more ambitious imaging ventures that seek to recover aside the species concentration, the gas temperature and pressure profiles [7], [6], [2]. Contrary to X-ray CT, data sets in CST tend to be limited due to instrumentation challenges [1], causing the image reconstruction approaches to depart from the typical Radon in-

version framework [9]. Existing algorithms are predominantly algebraic using inverse problem regularization tools, see for example the early work [10] and the more recent [11], [12], [13]. The use of statistical imaging methods is less by comparison, and some notable examples include the simulated annealing algorithm in [14] and the Bayesian estimation in [15], [8] and [12], who have developed algorithms for maximum a posteriori estimation assuming Gaussian priors and measurement likelihood probability density functions. As a detailed review of CST is beyond the scope of this paper, we mention that historical milestones and recent advances of the method are succinctly summarised in the recent review [16] and the book chapter [1]. To what concerns the novelty of this work we note that while spatial smoothness-imposing filters have been introduced and analysed in both the optimisation and statistical paradigms of the problem, to the best of our knowledge linear inequality constraints have not yet been considered in CST. As we elaborate next, our proposed optimisation-based scheme, inspired from the geophysical literature [17], enforces smoothness in the targeted image explicitly in the form of heuristically chosen basis functions as well as inequality constraints for positivity and boundedness by reformulating the model. In effect, this yields an *unconstrained inverse problem* and a *constrained model* that is directly amenable for a variety of alternative inverse problem formulations, e.g. sparsity promoting, total variation or levelset regularisation [18], [19]. Unfortunately, these advantages come at the cost of loosing the original model's linearity and thus a direct analytical inverse solution is no longer feasible, while the Bayesian setting results in a non-Gaussian posterior for the surrogate parameters, which complicates the inference calculations [8]. Moreover, the use of global basis functions as we advocated in [13] in reducing the dimensionality of the problem poses limitations to the statistical approaches that rely on computing image covariances and constructing prior densities from uncorrelated samples [15]. It should however be emphasised that whatever choice of basis is made, it is entirely heuristic, and a low-dimensional basis for the continuous concentration field with insignificant approximation error cannot be found without a priori knowledge of the targeted image. In dealing with infinite dimensional linear models, the approximation into a finite basis can be treated systematically by considering the resulting approximation error as a random variable [20].

To initiate the reader into the CST spectroscopic measurement models we provide a brief introduction to the fundamental relations, and fix our notation for the subsequent sections. Following the notation in [21] and assuming the beam intensity attenuates exponentially to the intervening medium's absorbance $\alpha \geq 0$, then the ratio of irradiance flux density at the detector I_d [Wcm^{-2}] to that at the source I_s at a distance L [cm] is given by Beer-Lambert's law

$$\frac{I_d}{I_s}\Big|_\nu = \mathrm{e}^{-\alpha(\nu)}, \tag{1}$$

then the spectral absorbance is

$$\alpha(\nu) = \int_L \mathrm{d}l\, k_\nu(x), \tag{2}$$

where k_ν [cm^{-1}] is the spectral absorption over the wavenumber perturbation $\nu \to \nu + \delta\nu$ and x is the spatial coordinate. If the light is measured at wavenumber ν [cm^{-1}] and x denotes the spatial coordinate then

$$k_\nu(x) = S_\nu(x;T)\,\phi_\nu(x;T,P,X)\,P_s(x), \tag{3}$$

where $S_\nu(x;T)$ [cm^{-2}atm^{-1}]is the temperature-dependent linestrength and $\phi_\nu(x;T,P,X)$ [cm] is the line-shape function at ν that depends both on the temperature and pressure of the gas and $P_s(x)$ [atm] is the partial pressure of the sth species, in this case the CO_2. To compute the spectral measurement we discretise the profiles of temperature, total gas pressure and mole fraction in a 2D spatial basis of functions defined on the optical plane to obtain $T(x)$ [K], $P(x)$ [atm] and the molar fraction function $X(x)$ respectively, since $P_s(x) = P(x)X(x)$. Importing data from the HITRAN database [22] at wavenumbers $\{\nu_1,\ldots,\nu_N\}$ in the vicinity of the measured frequency ν we can model the spectral absorbance of the species by approximating the profiles of S_ν and ϕ_ν at the resolution of the above bases using the definitions in [21]. In effect the spectroscopic measurement at ν becomes

$$\begin{aligned}\alpha(\nu) &\doteq \log \frac{I_s}{I_d}\Big|_{\nu_j} \\ &\approx \sum_{j=1}^{N} \int_L \mathrm{d}l\, S_{\nu_j}(x;T)\,\phi_{\nu_j}(x,\nu;T,P,X)\,P(x)\,X(x),\end{aligned} \tag{4}$$

while the approximation sign indicates that the relation is semi-empirical and depends on the availability and accuracy of the HITRAN data. Given measurements at M distinct wavenumbers $\{\alpha(\nu_1),\ldots,\alpha(\nu_M)\}$ when the temperature and total pressure profiles along the beam trajectory are known then Eq. (4) can be reduced to a weighted line integral for the sought concentration (mole fraction) function

$$\alpha(\nu_i) = \int_L \mathrm{d}l \sum_{j=1}^{N} \zeta^j(x,\nu_i)X(x), \quad i = 1,\ldots,M, \tag{5}$$

where $\zeta^j(x,\nu_i) = S_{\nu_j}(x)\phi_{\nu_j}(x,\nu_i)P(x)$ is a known weight function. Note that even when P and T are uniform, the ζ^j functions are not, thus Eq. (5) requires some model fitting techniques in order to extract the so-called 'path concentration data' along the beam when knowing the $\{\zeta^1,\ldots,\zeta^N\}$ and $\{\alpha(\nu_1),\ldots,\alpha(\nu_M)\}$ [16].

2. A LINEAR ATTENUATION MODEL FOR CONCENTRATION

We consider the inverse problem in CST for reconstructing the concentration image χ based on the measurement model Eq. (4) at a single wavenumber. Following the Radon transform paradigm [9], in a finite dimensional setting the integral equation leads to a discrete linear attenuation model

$$y = A\chi + \epsilon, \tag{6}$$

where $A \in \mathbb{R}^{m\times n}$ is the discretised measurement operator, $\chi \in \mathbb{R}^n$ is the discrete concentration parameter that is piecewise constant on the support of the model elements and ϵ is additive zero-mean noise. Based on Eq. (5) the measurement at the ith beam of the system is defined as

$$y_i \doteq \int_{L_i} \mathrm{d}l\, X(x), \quad i = 1,\ldots,m. \tag{7}$$

We are interested in the situations where the degrees of freedom n in the sought image exceed significantly the number of available data m, as this tends to be the usual setting in practical CST experiments [2], [3]. For $m \ll n$ the coefficients matrix in Eq. (6) attains a large null space and thus the model admits infinite

solutions, making the reconstruction of the concentration problematic. More precisely, if $m < n$ then A has m closely clustered singular values and, theoretically speaking, $n - m$ zero singular values. While its smallest non-singular value can be shown to be well above zero, see section 9.5 in [9] for the analytical definition of the singular values of the Radon transform and [13] for a numerical justification, the matrix is rank-deficient. To rectify the situation one typically applies some form of regularisation, usually of a Tikhonov-type [23], that stabilises the inversion and yields imaging with adequate stability and resolution. When the number of image parameters, e.g. voxels, n is large, Tikhonov (c.f. Eq. (24)) becomes computationally expensive, and challenging to optimise.

Our approach seeks to enforce some affine inequality constraints to bound the concentration to its admissible range $[0, 1]$, and to reduce the dimension of the default 'pixel-based' parameter space by projecting its image onto a subspace of global basis functions that are consistent with its expected smooth features. The methodology we propose has two distinct phases: We first model the concentration using a family of surrogate functions and then formulate the inverse problem with respect to a new set of parameters projected onto a low-dimensional subspace. This approach provides a straightforward way to transform the inverse problem into a low-dimensional unconstrained optimisation problem for a differentiable cost function. Its appeal lies primarily in the embedding of the inequality constraints into the model as oppose to constraining the inverse problem, its simplicity of implementation, and its computational robustness as it requires very little tuning. Although other alternatives exist within the framework of constrained optimisation algorithms, such as the projected gradients [24], active sets [25], linear programming and interior point methods [18], these algorithms are more complex and computationally expensive by comparison.

We describe our methodology by extending our previous work in [13], beginning with some important definitions. The subspace of bounded vectors in $\mathcal{S}_1 \subset \mathbb{R}^n$

$$\mathcal{S}_1 \doteq \{\chi \in \mathbb{R}^n \mid \ell \leq \chi \leq u\}, \quad \text{where} \quad 0 < \ell < u, \tag{8}$$

for some finite bounds ℓ and u. Further let a continuous and invertible, one-to-one mapping $v : \mathbb{R}^n \to \mathcal{S}_1$. Then there exists a unique vector of unconstrained parameters $\rho \in \mathbb{R}^n$ such that

$$\chi = v(\rho), \quad \forall x \in \mathcal{S}_1. \tag{9}$$

We aim to compute the projection of the high-dimensional ρ in a low-dimensional space of basis functions $\mathcal{S}_2 \subset \mathbb{R}^n$, such that

$$\mathcal{S}_2 \doteq \{Qr \mid r \in \mathbb{R}^s\}, \tag{10}$$

where $Q \in \mathbb{R}^{n \times s}$ is a matrix whose columns form an orthonormal basis of some feature functions $\{\phi_1, \ldots, \phi_s\}$ with $s \ll n$. This arrangement allows to formulate an inverse problem for the projection of the unconstrained vector of parameters ρ in $\mathcal{S}_2$, from which we ultimately obtain a constrained concentration image

$$\hat{\chi} = v(\Pi\hat{\rho}), \quad \text{where} \quad \Pi\rho = Q\rho, \tag{11}$$

for $\Pi : \mathbb{R}^n \to \mathcal{S}_2$ the associated projection matrix operator. This framework enforces affine inequality constraints on the admissible range of the image while it approximates the solution within a subspace of basis functions that are consistent with the expected features of the concentration image. For the targeted CST application the benefit of this approach is twofold: It constrains the concentration image within its intrinsic [0,1] bounds, and thereafter it allows to formulate the inverse problem for the logarithm of the concentration and thus making it more suitable to image multiscale concentration functions [17]. In the next section we present the foundation of our approach, namely the use of nonlinear surrogate functions that are suitable to model the constraints on the concentration image.

3. SURROGATE FUNCTIONS

For a fixed $\mathcal{S}_1$, we can find a re-parameterisation of $\chi \in \mathcal{S}_1$ via an invertible and analytic mapping

$$v : \mathbb{R} \to \mathcal{S}_1 \tag{12}$$

that we name the surrogate mapping. The invertibility provides v with the simultaneous surjectivity and injectivity, whereas the analyticity provides v with infinite differentiability. The most simple and practical manner to insure invertibility consists in considering mappings that are strictly monotonic.

We describe a practical method that can be used to obtain a surrogate mapping, by extending and generalising the priceedure in [17]. We focus initially on a surrogate mapping that satisfies the strict positiveness of the concentration. Thereafter, we show how we can reuse this surrogate mapping in order to obtain another surrogate mapping that bounds χ or its logarithm between two strictly positive bounds.

A. Strict positiveness.

If $\mathcal{S}_1$ is the set of the real numbers that are larger than a real number $\ell > 0$ then the following invertible and analytic function

$$v_{\mathrm{p}}(\rho; \ell) \doteq \mathrm{e}^{\rho} + \ell, \quad \forall\, \rho \in \mathbb{R},$$

is a model of the surrogate mapping Eq. (12). In particular, $v_{\mathrm{p}}(\rho; 0)$ is the inverse of the logarithmic function that has already been proposed as a model of the inverse mapping of Eq. (12) [17].

B. Boundedness.

Consider the following function

$$v_{\mathrm{s}}(\rho; \ell, u) \doteq \ell + \frac{u - \ell}{1 + \rho^{-1}}, \quad \forall\, \rho \in \mathbb{R},\ \forall\, \ell, u \in \mathbb{R},\ \ell < u.$$

If $\mathcal{S}_1$ is the set of the real numbers in the open interval of endpoints ℓ and u, with $0 < \ell$, then for a real number q such that $0 \leq q \leq u$ we can define the following invertible and analytic function

$$v_{\mathrm{b}}(\rho; \ell, q, u) \doteq v_{\mathrm{s}}(v_{\mathrm{p}}(\rho; \ell - q); \ell, u) = \ell + \frac{u - \ell}{1 + (\mathrm{e}^{\rho} + \ell - q)^{-1}}, \tag{13}$$

$\forall\, \rho \in \mathbb{R}$, so that

$$v_{\mathrm{b}}(\rho; \ell, \ell, u) = \ell + \frac{u - \ell}{1 + \mathrm{e}^{-\rho}}, \quad \forall\, \rho \in \mathbb{R},$$

is just another expression of a model of Eq. (12).

C. Logarithmic boundedness.

A particular case of boundedness occurs when we consider χ in an interval that is spanning over several orders of magnitude, or when the interval is extremely narrow. In such cases, it is more appropriate to bound the logarithm of χ. Indeed by noting that

$$\mathrm{e}^{\ell} < \chi < \mathrm{e}^{u} \iff \ell < \log \chi < u,$$

then by using a function

$$v_{\mathrm{l}}(\rho) \doteq \log \rho, \quad \forall\, \rho \in \mathbb{R},\ \text{s.t. } \rho > 0,$$

and the mapping v_{p} described in A, we can relate the boundedness of $\log \chi$ to the ordinary boundedness described in B. For $\rho = \log \chi$ it follows that $\rho = v_{\mathrm{l}}(v_{\mathrm{p}}(\rho; 0))$ and thus

$$v_{\mathrm{l}} \circ v_{\mathrm{p}} : \log \chi \mapsto v_{\mathrm{b}}(\rho; \ell, \ell, u).$$

Note that if $\mathcal{S}_1$ is the set of the real numbers that are strictly positive and whose logarithm is in the open interval with endpoints ℓ and u, then $v_{\mathrm{b}}(\rho; \ell, \ell, u)$ is not a model of the surrogate mapping Eq. (12), because v_{b} maps $\rho \in \mathbb{R}$ to $\log \chi$ instead of χ. However, since the range of $v_{\mathrm{b}}(\rho; \ell, \ell, u)$ is the interval with endpoints ℓ and u, since χ can be obtained from v_{b} univocally, then

$$v_{\mathrm{p}}(v_{\mathrm{b}}(\rho; \ell, \ell, u); 0)$$

always maps χ onto $\mathcal{S}_1$, and it is just another expression of a model of Eq. (12).

D. Generic surrogate mapping.

According to the constraints applied on χ, using the invertible and analytic mappings described in A-C, we can define a model of the surrogate mapping Eq. (12) as follows:

$$v(\rho) \doteq \begin{cases} v_{\mathrm{p}}(\rho; \ell) & \text{if } \mathcal{S}_1 = \{0 < \ell < \chi\} \quad \textbf{(14a)} \\ v_{\mathrm{b}}(\rho; \ell, \ell, u) & \text{if } \mathcal{S}_1 = \{0 < \ell < \chi < u\} \quad \textbf{(14b)} \\ v_{\mathrm{p}}(v_{\mathrm{b}}(\rho; \ell, \ell, u); 0) & \text{if } \mathcal{S}_1 = \{\ell < \log \chi < u\} \quad \textbf{(14c)} \end{cases}$$

Notice that Eq. (14a) is a special case of Eq. (14b). Indeed, if in Eq. (13) we replace v_{s} with the identity mapping $\mathrm{id}(v_{\mathrm{p}}) = v_{\mathrm{p}}$ then $v_{\mathrm{b}}(\rho; \ell, 0, u) = v_{\mathrm{p}}(\rho; \ell)$. Similarly, Eq. (14b) is a special case of Eq. (14c). Indeed, if $0 < \ell$ and we replace $\log \chi$ and v_{p} respectively with x and the identity mapping $\mathrm{id}(v_{\mathrm{b}}) = v_{\mathrm{b}}$ then $v_{\mathrm{p}}(v_{\mathrm{b}}(\rho; \ell, \ell, u); 0) = v_{\mathrm{b}}(\rho; \ell, \ell, u)$. For this reason, we can obtain the derivatives of v by considering only the derivatives of Eq. (14c). To keep the notation as general as possible, for all $\chi \in \mathcal{S}_1$ and $\rho \in \mathbb{R}^n$ we have

$$\chi = \mathrm{Y}(\rho) = [\mathrm{Y}_j(\rho)]_{j=1}^n, \quad \mathrm{Y}_j(\rho) \doteq v(\rho_j), \qquad \textbf{(15)}$$

and we notice that if $n = 1$ then Y reduces to v. The Jacobian matrix of Y is then shown to be

$$\mathrm{JY}(\rho) = \mathrm{D}\left[\frac{\mathrm{d}}{\mathrm{d}\rho_j} v(\rho_j)\right]_{j=1}^n, \qquad \textbf{(16)}$$

where D is an operator that transforms a vector ρ in the diagonal matrix whose main diagonal equals ρ. By applying the chain rule of differentiation on Eq. (14c) we obtain that

$$\begin{aligned} \frac{\mathrm{d}}{\mathrm{d}\rho_j} v(\rho_j) &= \frac{\mathrm{d}}{\mathrm{d}v_{\mathrm{b}}} v_{\mathrm{p}}(v_{\mathrm{b}}(\rho_j; \ell, \ell, u); 0) \\ &\quad \cdot \frac{\mathrm{d}}{\mathrm{d}v_{\mathrm{p}}} v_{\mathrm{s}}(v_{\mathrm{p}}(\rho_j; 0); \ell, u) \frac{\mathrm{d}}{\mathrm{d}\rho_j} v_{\mathrm{p}}(\rho_j; 0) \\ &= \frac{v_{\mathrm{p}}(v_{\mathrm{b}}(\rho_j; \ell, \ell, u); 0)(u - \ell) v_{\mathrm{p}}(\rho_j; 0)}{(1 + v_{\mathrm{p}}(\rho_j; 0))^2}, \end{aligned}$$

therefore in general the derivative of v is

$$\frac{\mathrm{d}}{\mathrm{d}\rho_j} v(\rho_j) = \begin{cases} v_{\mathrm{p}}(\rho_j; 0) & \text{if Eq. (14a)} \\ \frac{(u-\ell)\, v_{\mathrm{p}}(\rho_j; 0)}{(1+v_{\mathrm{p}}(\rho_j; 0))^2} & \text{if Eq. (14b)} \\ \frac{v(\rho_j)\,(u-\ell)\, v_{\mathrm{p}}(\rho_j; 0)}{(1+v_{\mathrm{p}}(\rho_j; 0))^2} & \text{if Eq. (14c)} \end{cases}. \qquad \textbf{(17)}$$

4. THE PROJECTED INVERSE PROBLEM

In a previous work we have devised an approach that involved reducing the dimensionality of the sought image by projecting it into a smooth basis of orthogonal functions and thereafter regularising the projected problem [13]. We now attempt to extend this framework by introducing affine inequality constraints on the values of the image. Having defined the surrogate functions for the concentration image we set out to cast the inverse problem with respect to the surrogate parameters ρ. To stabilise the inversion we reduce the degrees of freedom in the resulting inverse problem, by adopting the following assumption. If we consider a projection $\Pi\rho \in \mathcal{S}_2$ then we seek to reconstruct χ when its corresponding surrogate image $\rho = v^{-1}(\chi)$ satisfies

$$\frac{\|\rho - \Pi\rho\|}{\|\rho\|} < 1,$$

since ultimately our approach is restricted to reconstructing only the $\Pi\rho$ of x. The choice of basis functions Q involved in the projection $\Pi = Q(Q^TQ)^{-1}Q^T$ is made to impart some level of smoothness to the expected image, as this is consistent with the expected profile of the concentration and plume velocity. From the surrogate form of model Eq. (6),

$$y = Av(\rho) + \epsilon, \qquad \textbf{(18)}$$

linearising at point $\rho^{(i)}$ yields

$$y \approx A\left(v(\rho^{(i)}) + \mathrm{JY}(\rho^{(i)})(\rho - \rho^{(i)})\right) + \epsilon, \qquad \textbf{(19)}$$

and thus imposing $\Pi\rho = Qr$ and setting

$$y(\rho^{(i)}) = y - Av(\rho^{(i)}) + A\mathrm{JY}(\rho^{(i)})\rho^{(i)}, \quad K(\rho^{(i)}) = A\mathrm{JY}(\rho^{(i)}),$$

we arrive at the ith projected surrogate model

$$y(\rho^{(i)}) = K(\rho^{(i)})Qr + \tilde{\epsilon}, \qquad \textbf{(20)}$$

with the noise $\tilde{\epsilon}$ now including also the projection approximation error. In the context of the Gauss-Newton algorithm, an image can be reconstructed iteratively by solving the regularised problems

$$\hat{r}^{(i+1)} = \underset{r \in \mathbb{R}^s}{\operatorname{argmin}} \left\{ \left\| y(\rho^{(i)}) - K(\rho^{(i)})Qr \right\|^2 + \lambda^2 \left\| r - r^{(i)} \right\|^2 \right\}, \qquad \textbf{(21)}$$

for $i = 1, 2, \ldots$ where λ is a regularisation parameter, $\Pi\rho^{(i)} = Qr^{(i)}$, and JY the Jacobian of v, can be obtained from the formulas Eq. (14a)-Eq. (14c). As shown in [13] the choice of the reduced basis can render the resulted coefficient matrix $K(\rho)Q$ rank deficient as functions with global support may introduce linear dependencies in the measured integrals. We note that the sequence of regularised least squares problems in Eq. (21) are equivalent to those addressed by the Levenberg-Marquardt algorithm which iteratively dampens the null space of the system's Hessian matrix and computes the updated solution within a trust region centred at the previous estimate. For these reasons a $\lambda > 0$ is required. As the data are corrupted by the additive and approximation errors, as explained in [26], it is imperative that iterations are terminated before the algorithm converges to the least squares solution. Although in the Levenberg-Marquardt the regularisation parameter is adjusted in each iteration, in our implementation we maintain its value fixed while we control the progress of the iterations using Morozov's discrepancy principle [25]. As we discuss in brief below, a near-optimal value of λ

can be efficiently traced based on a heuristic criterion originally proposed in [13]. Ultimately, the reconstructed concentration image can be obtained from Eq. (21) by

$$\hat{\chi}^{(i)} = v(Q\hat{r}^{(i)}). \tag{22}$$

For the sake of comparison, we also compute the constrained linear least squares inverse problem for the original parameters

$$\hat{\chi}_c = \underset{\chi\in\mathbb{R}^n}{\operatorname{argmin}}\left\{\left\|\begin{pmatrix} A \\ \lambda R\end{pmatrix}\chi - \begin{pmatrix} y \\ \lambda R\chi_0\end{pmatrix}\right\|^2\right\}, \quad \text{for} \quad \begin{cases}\chi > 0 \\ \ell \le \chi \le u\end{cases} \tag{23}$$

using an active sets algorithm as this is implemented in Matlab's functions `lsqnonneg` and `lsqlin` for the nonnegative and box constrained cases respectively [28]. The unconstrained instance of Eq. (23) constitutes to solving the generalized Tikhonov problem

$$\hat{\chi}_t = (A^TA + \lambda^2 R^TR)^{-1}(A^Ty + \lambda^2 R^TR\chi_0), \tag{24}$$

for an initial guesstimate χ_0. The comparison with Tikhonov solutions is appropriate for a number of reasons. Tikhonov regularisation is among the most popular regularisation strategies in inverse problems and CST in particular. Moreover, its analytic formulation allows for a direct application to a default constrained optimisation solver, such as those included in Matlab, from where we compute images for comparison. Thirdly, the Tikhonov problem bares an evocative resemblance to the maximum a posteriori estimator in the Bayesian inverse problem, subject to a suitably smooth prior density [8], [15], and lastly upon the appropriate choice of the regularization matrix and parameter it can impose the required smoothness in the unknown image profile, which makes is compatible to our method. Note however that our scheme enforces smoothness explicitly by selecting a (particular) basis for the projection in Eq. (11), while Tikhonov imposes smoothness indirectly by correlating the values of the image according to their distance.

5. NUMERICAL RESULTS

In this section we present some results obtained from numerical simulation experiments. Data were computed from Eq. (6) based a high resolution grid with $n = 10000$ elements for a target concentration image χ and then infused with zero-mean Gaussian noise at a standard deviation of 10% of each data value. The model was constructed to simulate the measurements of the FLITES system [3] based on a beam arrangement of six projection angles at $\{0, 30, 60, 90, 120, 150\}$ degrees, each comprising twenty one parallel beams, as shown in the schematic of figure 1. To investigate the performance of our methods in reconstructing concentration profiles with low and high spatial variation we consider two distinct tests with targets χ_l^* and χ_h^*, as sums of Gaussian functions

$$\chi^*(x) = \sum_{i=1}^{5}\chi_i(x), \quad \chi_i(x) = |\chi_i|\exp\left\{\frac{-(x-x_i')^2}{2\sigma_i^2}\right\}, \tag{25}$$

where the specific amplitudes $|\chi|$, centres x' and spreads σ are tabulated in table 1.

To assess the quality of the reconstructed images $\hat{\chi}$ and the convergence of the algorithm we compute the standard relative errors for the data and images, which from Eq. (22) are given by

$$\eta_D(\hat{\chi}) \doteq \frac{\|y - A\hat{\chi}\|}{\|y\|}, \quad \text{and} \quad \eta_I(\hat{\chi}) \doteq \frac{\|\hat{\chi} - \Pi\chi^*\|}{\|\Pi\chi^*\|}, \tag{26}$$

Table 1. Specifications of the synthetic high-variation and low-variation concentration profile χ_h^* and χ_l^* respectively in Eq. (25).

σ_i	$\lvert\chi_i\rvert$ in χ_h^*	$\lvert\chi_i\rvert$ in χ_l^*	$x_i' \equiv (x_i, y_i)$
0.0004	0.6	0.15	(0,0)
0.001	1.0	0.10	(0,-0.1)
0.005	0.4	0.15	(-0.2,0.1)
0.01	0.8	0.05	(0.1,0.1)
0.002	0.2	0.01	(-0.15,-0.15)

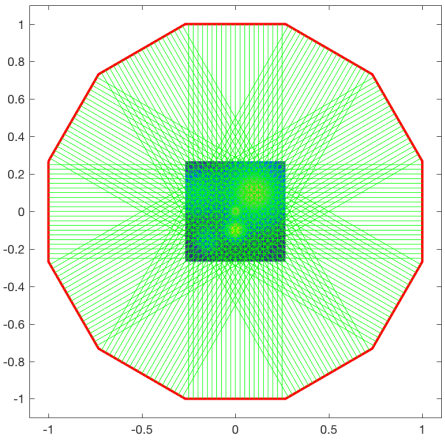

Fig. 1. A schematic of the physical FLITES ring with the 126 beams equally distributed in six projection angles, indicating also the positioning of the imaging domain. The scale of the drawing is 1 unit for 3.5 m.

recalling that as we showed in [13], due to the subspace projection induced information loss the 'best' image we can hope to recover for a target χ^* is $\Pi\chi^*$.

The high variation concentration target is bounded by $3 \times 10^{-4} \leq \chi_h^* \leq 1$ and for this test we have used a subspace of 225 radial basis functions, orthonormalized through the Gram-Schmidt process [28]. In turn this led to a projection approximation error of $\|\rho_h^* - \Pi\rho_h^*\|/\|\rho_h^*\| \approx 0.12$ which sets the lower bound of the image reconstruction error. We run the algorithm for the three types of surrogate mappings and compare the results with that obtained from the unconstrained and constrained forms of the Tikhonov solution in Eq. (24) and Eq. (23) respectively, for a smoothness imposing regularisation matrix $R \in \mathbb{R}^{n\times n}$ based on the definition in [1] and a uniform prior guess χ_0. For the inverse problem the model Eq. (6) was discretised on a courser grid comprising $n = 3600$ voxels on which we have also approximated the target and its projection to aid the visual assessment of the reconstructions and the evaluation of the error measures in Eq. (26). The images in figure 2, show that the performance of our scheme is superior to that of the unconstrained Tikhonov method, which yields irrational negative concentration values and is comparable to the constrained Tikhonov solutions. The images of the proposed method correspond to running 5 Gauss-Newton iterations on the projected inverse problem for the surrogate parameters with a value of λ around 10^{-2}. In this 'high-variation' benchmark the three surrogate formulations perform equally well, converging almost simultaneously after the first 5 iterations as shown in the left column of figure 4. The unconstrained Tikhonov solution with the same data and a manually adjusted $\lambda = 1$ attains a smaller relative data error at $\eta_D = 2.2 \times 10^{-4}$ but the relative error in the image is much higher at $\eta_I = 0.37$. To minimise bias in the comparison all initial prior guess images were chosen to be positive and homogenous. The nonnegative and bounded Tikhonov solutions were computed based on the Matlab commands after 3400 and 1893 iterations respectively to relative data errors 0.013 and 0.042, and image errors at 0.244 and 0.217. It is also worthwhile mentioning that for the coarse grid with 3600 parameters, executing `lsqnonneg` and `lsqlin` on a 3.4 GHz Intel Core i7 Mac with 32GB RAM took about 16 and 11 minutes respectively while the 5 iterations of our algorithm took on average for all three surrogates about 5 seconds. Indicatively, we note that the assembling and othogonalization of the projection bases matrix Q took about 4 seconds while the switching between original and surrogate parameters as in Eq. (22) required less than a second.

To investigate the utility of our method in reconstructing concentration profiles of low variation we perform a similar simulation on a target χ_l^* whose values are in the range $1.5 \times 10^{-5} \leq \chi_l^* \leq 0.16$ as shown in 3. Keeping the signal to noise ratio fixed, we compute regularisation values and control the number of iterations using the discrepancy principle after 5 iterations we arrive at the images illustrated in figure 3 and the convergence plots for η_D and η_I on the right hand column of figure 4. Similar to the 'high-variation' case results our methodology seems to perform better than unconstrained Tikhonov regularisation where $\eta_I = 0.30$ and $\eta_D = 1.15 \times 10^{-4}$, despite that the subspace projection error is larger, see for example the images in the top row of figure 3. This set of results reveals also that in this case bounding the values of the image or indeed the logarithm of the image improves the reconstruction, both in terms of the spatial resolution of the images but also in

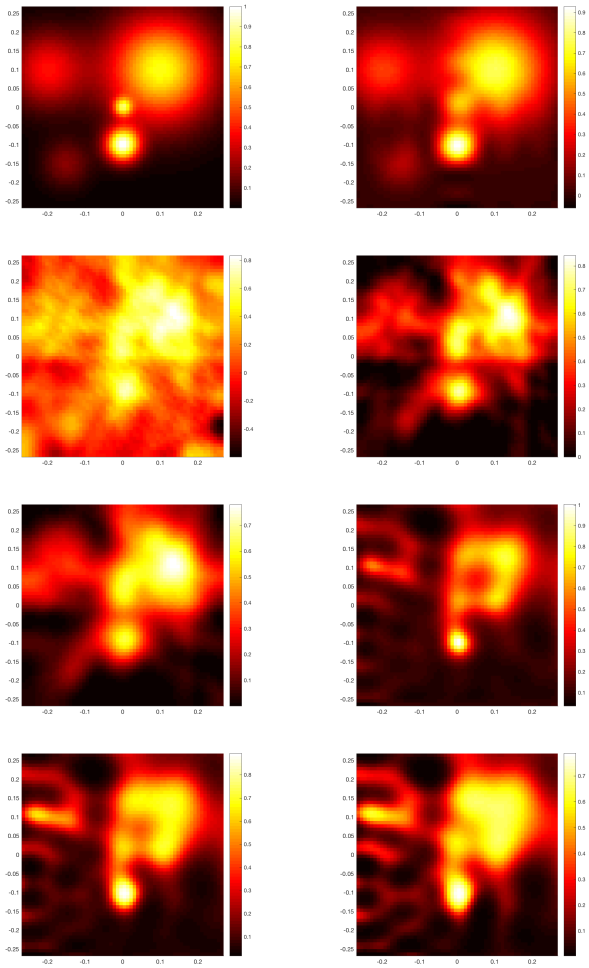

Fig. 2. At the top row the high-variation target image χ_h^* in a 60×60 square pixel grid and its projection $\Pi\chi_h^*$ showing some approximation error. Below the smooth unconstrained Tikhonov solution, and the nonnegative Tikhonov solution, and at the next row the bounded Tikhonov solution and to its right the positive image obtain from our method after 5 Gauss-Newton iterations. At the final row the images based on boundedness and logarithmic boundedness surrogate functions after 5 iterations. Aside the unconstrained Tikhonov that yields negative concentration values, the constrained solutions are of similar quality with relative image errors of about $\eta_I = 0.25$.

terms of the convergence of the reconstruction algorithm. The graphs at the right column of figure 4 show that the bounded and logarithmically bounded iterations converge faster than the positivity case, while the graph of the relative image error shows again the issue of divergence in the solution after the first 6 or so iterations highlighting the need for a stoping criterion. In terms of the image errors, those of our algorithm are very similar, if not marginally better, to those of the constrained solvers in Matlab at $\eta_I = 0.18$ and $\eta_I = 0.20$ for the positive and box bounded solutions compared to $\eta_I = 0.24$ and $\eta_I = 0.23$ obtained by `lsqnonneg` and `linlsq` respectively. In terms of the relative data errors, the unconstrained Tikhonov was again the lowest at $\eta_D = 1.15 \times 10^{-4}$ while those of the constrained version were similar to those obtained for our algorithm (c.f. figure 4) at $\eta_D = 0.027$ and $\eta_D = 0.064$ for the nonnegative and bounded cases. In terms of the computational complexity, the Matlab solvers take in excess of 10 minutes each for 3030 iterations for `lsqnonneg` and 5388 iterations in `linlsq`.

A. Tuning the regularisation parameter

In [13] we have proposed a heuristic method for choosing the regularisation parameter for the linear projected inverse problem, without any surrogate variable transformation. According to this we compute the linearised solution Eq. (21) on a sequence of logarithmically equidistant values of λ, ranging from the largest singular value of KQ to its smallest non-zero singular value. We then compute the norm of the difference between every two successive solutions and plot them against the midpoint average values of the regularisation parameter. As we argued in [13], given the rank deficiency of the projected, and now surrogate projected model we expect the optimal value of λ near the minimum of the graph within that range of λ values

$$\Delta\hat{r}(\lambda_j) = \|\hat{r}(\lambda_i) - \hat{r}(\lambda_{i+1})\|, \quad \lambda_j = \frac{1}{2}(\lambda_i + \lambda_{i+1}). \tag{27}$$

To verify and demonstrate this criterion we compute the solutions at 500 regularisation parameters and plot the running difference norm $\Delta\hat{r}$ against λ in figure 5, along with the norm of the discrepancy between each λ-dependent solutions to the true projected solution $\Pi\chi^*$. The graphs, which refer to the bounded and logarithmically bounded surrogate problems for the two test cases χ_h^* and χ_l^* show that the two curves attain a minimum around the same value of λ, e.g. close to 10^{-2}. To aid stability the model Eq. (6) is scaled so that $\|A\| = 1$, and since Q has orthonormal columns the maximum singular value of $KQ = AJYQ$ is around 1. The time required to solve these problems for each λ was about 1 minute, since despite having to solve 500 different instances, the systems were low-dimensional.

6. REAL DATA RECONSTRUCTION

At the FLITES experiment an optical imaging ring has been constructed [3] to provide 126 simultaneous measurements of CO_2 equally arranged in 6 projection angles, using the calibration-free 2f/1f wavelength modulation spectroscopy technique (TDLS-WM) [5]. The light sources and sensors are positioned perimetrically at a 12-sided ring of 7 m in diameter. In this section we present some reconstructions from measurements obtained from controlled phantom experiments using this system. The data correspond to two circular, almost homogenous carbon dioxide plumes arranged diagonally with respect to the centre of the computational domain, one at 40 cm diameter and the other at

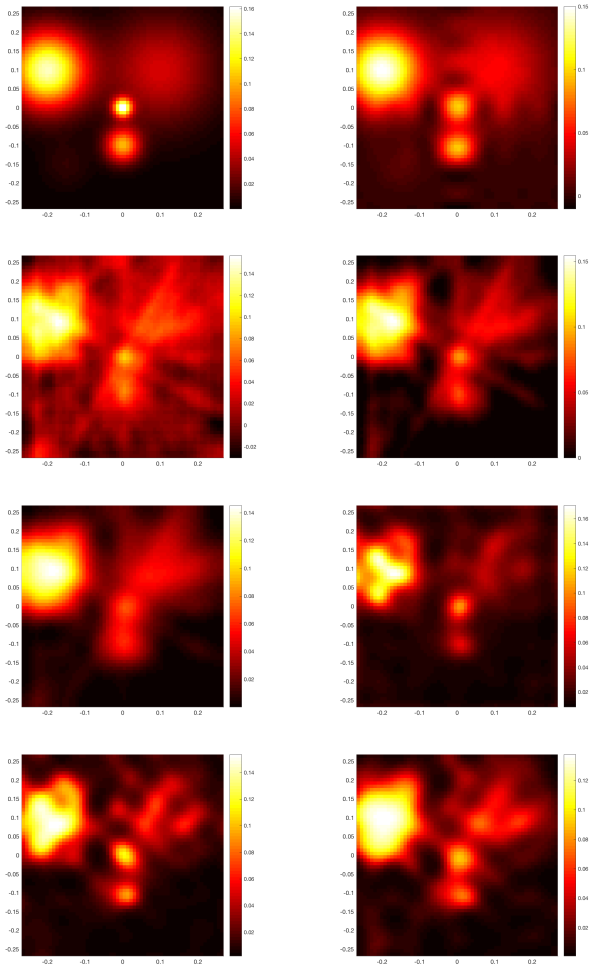

Fig. 3. At the top row the low-variation target image χ_l^* in a 60×60 square grid and its projection $\Pi\chi_h^*$ indicating some distortion due to the subspace approximation. Below the smooth unconstrained Tikhonov and the nonnegative Tikhonov solutions, while in the next row we plot the bounded Tikhonov solution and to its right the positive image obtain from our method after 5 Gauss-Newton iterations. At the final row the respective images based on boundedness and logarithmic boundedness surrogate functions.

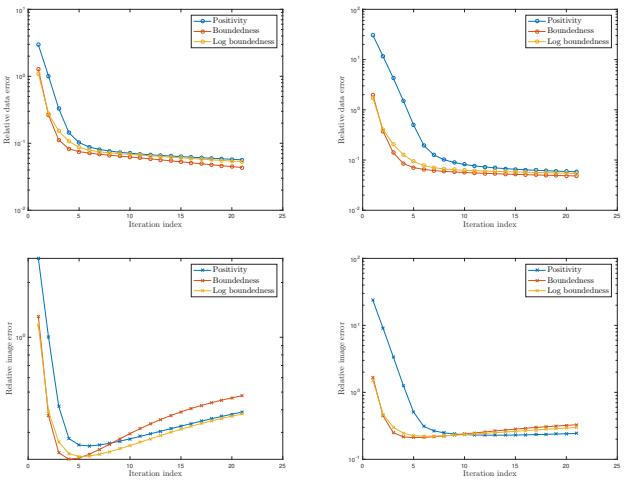

Fig. 4. At the top the relative data error $\eta_D(\hat{\chi})$ reduction plots at each Gauss-Newton iteration for the three surrogate transformations during the χ_h^* (left) and χ_l^* (right) tests. Below the corresponding curves for the image errors $\eta_I(\hat{\chi})$ for the same tests and surrogates. The graphs demonstrate the requirement for terminating the iterations in order to avoid fitting the noise into the images, i.e. note the divergence in the bottom row after iteration 6, while the data errors in the upper row continue to reduce. Comparing between the two tests, the graphs to the left show that convergence and error reduction is similar for all three choices of surrogates, while those to the right for χ_l^* show that the boundedness and logarithmic boundedness iterations converge much faster than the positivity case. The errors are computed based on the formulas Eq. (26).

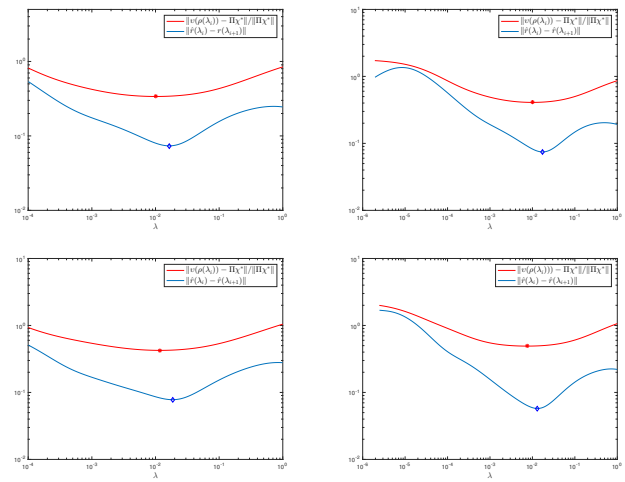

Fig. 5. Choosing the regularisation parameters. The range of values for λ beginning at the smallest singular value of KQ before the rank deficiency jump in the spectrum and ending its largest singular value that was normalised to be 1. The star marker on the red curve denotes the optimal value of λ while the diamond is the computed minimum of the curve in Eq. (27). Note that normally only the blue curve can be computed, and the red curve is plotted here merely for validation.

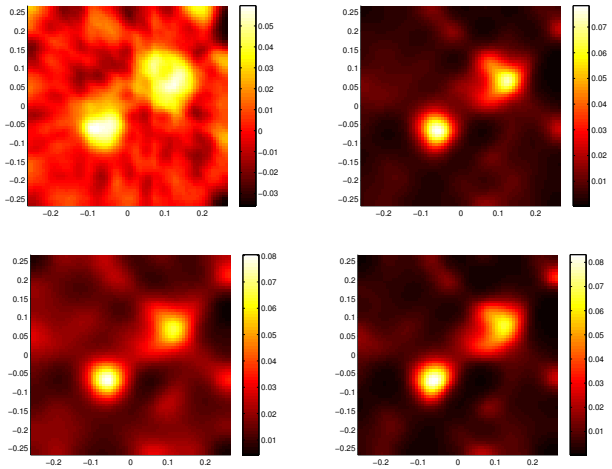

Fig. 6. At the top row the high-dimensional Tikhonov solution and the image reconstruction with the positiveness surrogate. Below the corresponding images with boundedness and logarithmic boundedness constraints.

60 cm. The concentration of the gas was measured to be approximately 6% for both plumes, using a flue gas analyser (Kane 455). The optical signal was generated using a master oscillator power amplifier configuration. The seed laser was an Eblana Photonics Multi Quantum Well Distributed Feedback (DFB) laser (EP1997-DMB01-FM), whose output power could be amplified to a maximum of 2 W using a Thulim Doped Fibre Amplifier designed and manufactured by the University of Southampton [27]. The output from the amplifier is distributed around the hosting ring using a bespoke optical fibre network, providing 126 optical beams to be directed through the imaging space. The seed laser current was modulated at 5 Hz and 100 kHz for the purpose of using the 2f/1f calibration-free tunable diode laser spectroscopy with wavelength modulation technique [5]. The individual photo-diode outputs from the 126 channels were recorded using an NI-PXI-6366 data acquisition (DAQ) board at 2MS/s. As the DAQ only allows 8 channels to be recorded simultaneously an NI-PXI 2530B multiplexor was used to consecutively switch between the 126 channels, giving a full data acquisition rate of about 0.3 Hz. The recorded signals were demodulated using a bespoke LabVIEW based lock-in amplifier and the path-integrated mole-fraction measurements were obtained using the methodology described in [16].

In the image reconstruction we have used the same surrogate formulations as in the simulated cases, although in this case we have projected the surrogate problem into a basis of 64 discrete cosine basis functions. The resulted images after 4 Gauss-Newton iterations are presented in figure 6, for the three different surrogate formulations at a relative data error of around $\eta_D = 0.6$. Compared to the smooth Tikhonov image, the iterative results appear to be quantitatively and qualitatively superior. Due to the significant levels of noise in the data the distinction in the diameter of the two plumes is not very profound in these images.

7. CONCLUSIONS

This paper presents an algorithmic framework for concentration imaging in chemical species tomography with linear inequal-

ity constraints. The key aspect of our approach is the use of surrogate functions that introduce these constraints within the forward model by re-parameterisation leading into an unconstrained inverse problem formulation. This constrained model is then projected into a low-dimensional subspace to improve the stability of the inversion when having limited tomographic data. The resulting problem was then addressed using the Gauss-Newton algorithm and results from simulated and real measurements demonstrated that the spatial resolution of the images is significantly enhanced compared to unconstrained, Tikhonov solutions with smoothness imposing regularisation. Compared to solving the unprojected inverse problem with non-negativity and bound constraints using constrained optimisation software our method yields images of comparable quality at a small fraction of the time. Our computational results indicate also that bounding the image's value or its logarithm from above and below offers faster convergence and better accuracy in concentration functions with low spatial variation, although a stopping criterion is needed in order to terminate the iterations before the solution diverges. Compared to unconstrained regularised solvers the advantage of our method is both quantitative and qualitative as the concentration levels are recovered with better accuracy while at the same time the features of the images are enhanced avoiding to a large degree unwanted blurring effects.

8. FUNDING INFORMATION

We acknowledge EPSRC for funding this work in the context of FLITES : 'Fibre-Laser Imaging of gas Turbine Exhaust Species' project. (EP/J002151/1)

9. ACKNOWLEDGMENTS

We are grateful to Victor Archilla and coworkers at INTA Madrid for facilitating the phantom tests, and Mark Johnson of Rolls Royce for helpful discussions on jet engine combustion and emissions.

REFERENCES

1. McCann H, Wright P and Daun K 2015, *Industrial Tomography: Systems and Applications*, Elsevier.
2. Ma L, Li X, Sanders S T, Caswell A W, Roy S, Plemmons D H, and Gord J R, 2013, *50-kHz-rate 2D imaging of tepmerature and H20 concentration at the exhaust plane of a J85 engine using hyperspectral tomography*, Optics Express, **21(1)**, 1152-1162.
3. Wright P, Mccormick D, Kliment J, Ozanyan K, Tsekenis S, Fisher E, McCann H, Archilla V, Gonzalez-Nunez A, Johnson M, Black J, Lengden M, Wilson D, Johnstone W, Feng Y, and Nilsson J, 2016, *Implementation of non-intrusive jet exhaust species distribution measurements within a test facility*, IEEE Aerospace Conference.
4. Twynstra M J and Daun K J, 2013, *Laser-absorption tomography beam arrangement optimisation using resolution matrices*, Applied Optics, **51**, 7059-7068.
5. Rieker G B, Jeffries J B, and Hanson R K, 2009, *Calibration-free wavelength-modulation spectroscopy for measurements of gas temperature and concentration in harsh environments* Applied Optics, **48**(29), 5546-5560
6. Ma L and Cai W, 2008, *Numerical investigation of hyperspectral tomography for simultaneous temperature and concentration imaging*, Applied Optics **47(21)**, 3751-3759.
7. Cai W and Kaminski F C, 2014, *A tomographic technique for the simultaneous imaging of temperature, chemical species, and pressure in reactive flows using absorption spectrocsopy with frequency-agile lasers*, Applied Physics Letters, **104**.
8. Grauer S J, Tsang R W and Daun K J, 2017, *Broadband chemical species tomography: Measurement theory and a proof-of-concept emission detection experiment*, J. of Quant. Spectrosc. Radiat. Transf., **198**, 145-154.
9. Bertero M and Boccacci P, 2002, *Introduction to inverse problems in imaging*, Institute of Physics.
10. Torniainen E D, Hinz A K and Gouldin C F, 1998, *Tomographic analysis of unsteady, reactive flows: numerical investigation*, AIAA Journal, **36(7)**, 1270-1278.
11. Terzija N and McCann H, 2010, *Wavelet-based image reconstruction for hard-field tomography with severely limited data*, IEEE Sensors Journal, **11(9)**, 1885-1893.
12. Daun K J 2010, *Infrared species limited data tomography through Tikhonov reconstruction* J. Quant. Spectrosc. Radiat. Transf. **111**, 105-115.
13. Polydorides N, Tsekenis A, McCann H, Archilla V-P and Wright P 2016, *An efficient approach for limited-data chemical species tomography and its error bounds*, R. Soc. A **472**, 2187.
14. Cai W and Kaminski F C, 2014, *Multiplexed absorption tomography with calibration-free wavelength modulation spectroscopy*, **104**
15. Grauer S J, Hadwin P J and Daun K J, 2016, *Bayesian approach to the design of chemical species tomography experiments*, Applied Optics, **55(21)**, 5772-5782.
16. Cai W, and Kaminski F C, 2017, *Tomographic absorption spectroscopy for the study of gas dynamics and reactive flows*, Progress in Energy and Combustion Science, **59**.
17. Commer M and Newman A G 2008, *New advances in three-dimensional controlled-source electromagnetic inversion*, Geophys. J. Int. **172**, 513-535.
18. Boyd S and Vandenberghe L 2004, Convex optimisation, *Cambridge University Press*.
19. Twynstra M G, Daun K J and Waslander S L, 2014, *Line-of-sight-attenuation chemical species tomography through the level set method*, J. Quant. Spectrosc. Radiat. Transf., **143**, 25-34.
20. Kaipio J and Somersalo E, 2007, *Statistical inverse crimes: Discretisation, model reduction and inverse crimes*, Computational and Applied Mathematics, **198(2)**, 493-504.
21. Hanson R K, Spearrin R M, Goldenstein C S, 2016, *Spectroscopy and optical diagnostics for gases*, Springer.
22. High Resolution Transmission database, www.hitran.org
23. Hansen P C, 2002, *Rank-deficient and discrete ill-posed problems: Numerical aspects of linear inversion*, SIAM.
24. Bertsekas D P 1982, *Projected Newton methods for optimisation problems with simple constraints*, SIAM J. Contr. Opt. **20**(2), 221-246.
25. Gill P E, Murray W, and Wright M H 1981, Practical Optimization, *Academic Press*, London, UK.
26. Hanke M 1997, *A regularizing Levenberg - Marquardt scheme, with applications to inverse groundwater filtration problems*, Inverse problems **13**(1), 79-95.
27. Feng Y, Nilsson J, Jain S, May-Smith T C, Sahu J K, Jia F, Wilson D, Lengden M and Johnstone W, 2014, *LD-seeded thulium-doped fibre amplifier for CO_2 measurements at 2 μm*, 6th Europhoton Conference (EPS-QEOD).
28. Matlab and Optimisation Toolbox, Release 2016a, The MathWorks, Inc., Natick, Massachusetts, United States.